Chapter 9
Hollow or Yolk–Shell-Type Photocatalyst

The photocatalytic efficiency of bulk semiconductor particles generally suffers from poor diffusion efficiency of photo-generated carriers from the inside to the surface and low absorption efficiency to the incident light. The introduction of cavity inside the semiconductor particle has been proven effective to form accessible active sites throughout the bulk particle and enhance the light absorption efficiency through multiple scattering effects. Moreover, through reasonably spatial arrangement of different components in a single particle, the hole–electron separation degree can be enhanced, and functions such as plasmon resonance absorption and magnetic separation can be extra assembled. In this chapter, we mainly discuss the synthesis and characteristics-tuning of hollow-, yolk–shell-, hierarchical-, and tubular-type photocatalyst and the structural effect on the photocatalytic performance.

9.1 Synthesis

The generation of void inside the semiconductor can be achieved mainly through non-template (Kirkendall, Ostwald ripening) and hard-template (silica, carbon, polymer colloids) routes [1–3]. Both methods can form cavitory semiconductors with versatile structures and highly tunable dimensions concerning core, shell, and void.

9.1.1 Non-template Route

Ostwald ripening is the most commonly used strategy for non-template synthesis of cavitory semiconductor [2, 4, 5]. A typical example is the formation of hollow anatase TiO_2 nanospheres using TiF_4 as the precursor in aqueous system and under hydrothermal conditions (Fig. 9.1) [2]. Inner nanospace and highly organized

J. Zhang et al., *Photocatalysis*, Lecture Notes in Chemistry 100,
https://doi.org/10.1007/978-981-13-2113-9_9

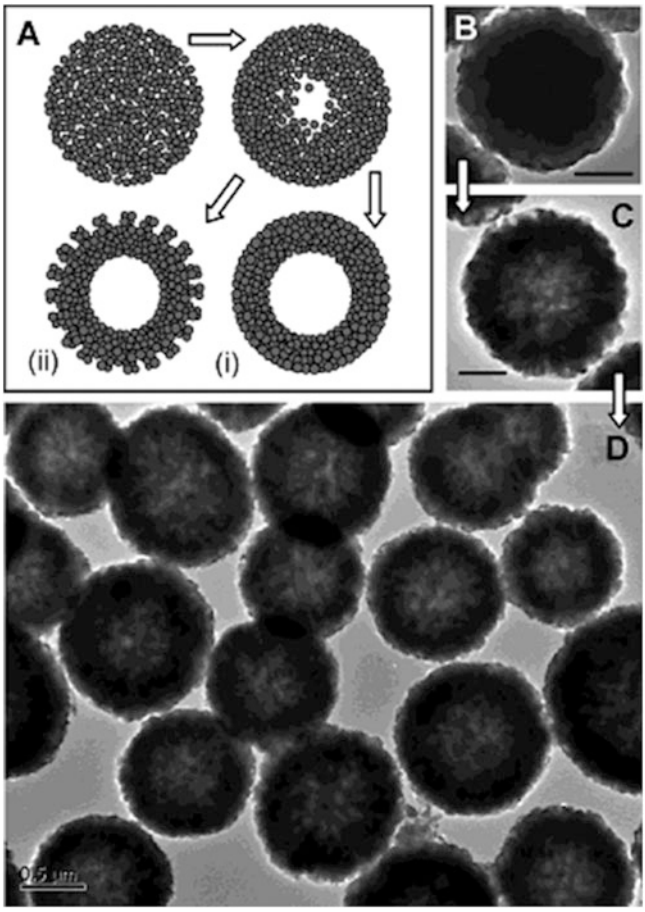

Fig. 9.1 (**a**) Schematic illustration (cross-sectional views) of the ripening process and two types (i & ii) of hollow structures. Evolution (TEM images) of TiO_2 nanospheres synthesized with 30 mL of TiF_4 (1.33 mM) at 180 °C with different reaction times: (**b**) 2 h (scale bar = 200 nm), (**c**) 20 h (scale bar = 200 nm), and (**d**) 50 h (scale bar = 500 nm) (Reprinted with the permission from ref. [2]. Copyright 2004 American Chemical Society)

crystallites in the shell structure and surface regions can be created with a wide range of controlling parameters. The interior void enlarges with the prolonging ripening process.

Bian et al. prepared mesoporous titania spheres with tunable chamber structure, where $TiOSO_4$ as the titania precursor was solvothermally reacted in glycerol, alcohol, and ethyl ether [6]. Judicious choice of the alcohol molecules (e.g., methanol, ethanol, and propanol) and reaction time affords the synthesis of spheres with adjustable morphology, size, and interior structure that is tunable from solid, sphere-in-sphere, to hollow. The formation of such spheres may involve aggregation of titania building clusters into spheres and their subsequent reaction, dissolution, and

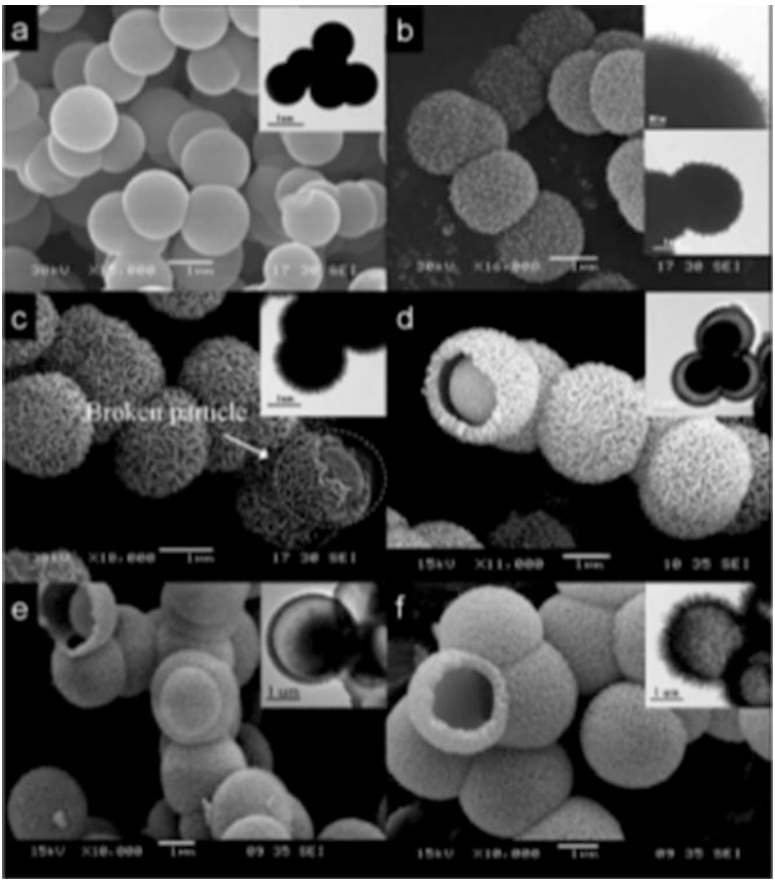

Fig. 9.2 SEM and TEM (insets) images of the titania spheres synthesized for (**a**) 1/24, (**b**) 0.5, (**c**) 1, (**d**) 2, (**e**) 7, and (**f**) 14 days, showing transiting interior structure from dense, to sphere-in-sphere, to hollow and surface morphology from smooth to prickly (Reprinted with the permission from ref. [6]. Copyright 2007 American Chemical Society)

redeposition process. Specially, during the solvothermal condition, etherifying reactions between alcohol and glycerol produce water continuously. Titania building clusters may be generated through alcoholysis reaction or hydrolysis–condensation reactions of $TiOSO_4$. Solid spheres first formed from the clusters aggregation, which contain a large number of hydrolyzable ligands due to slow reaction kinetics. Water continuously produced from the etherifying reactions further drives the hydrolysis–condensation reaction forward, leading to the dissolution and rearrangement of the surface building clusters (Fig. 9.2).

Hierarchical macro-/mesoporous titania can be prepared without the addition of templates or auxiliary additives at room temperature by the simple dropwise addition of tetrabutyl titanate (TBOT) to pure water and then calcined at various temperatures (Fig. 9.3) [7]. Firstly, the contact between the TBOT droplets and distilled water

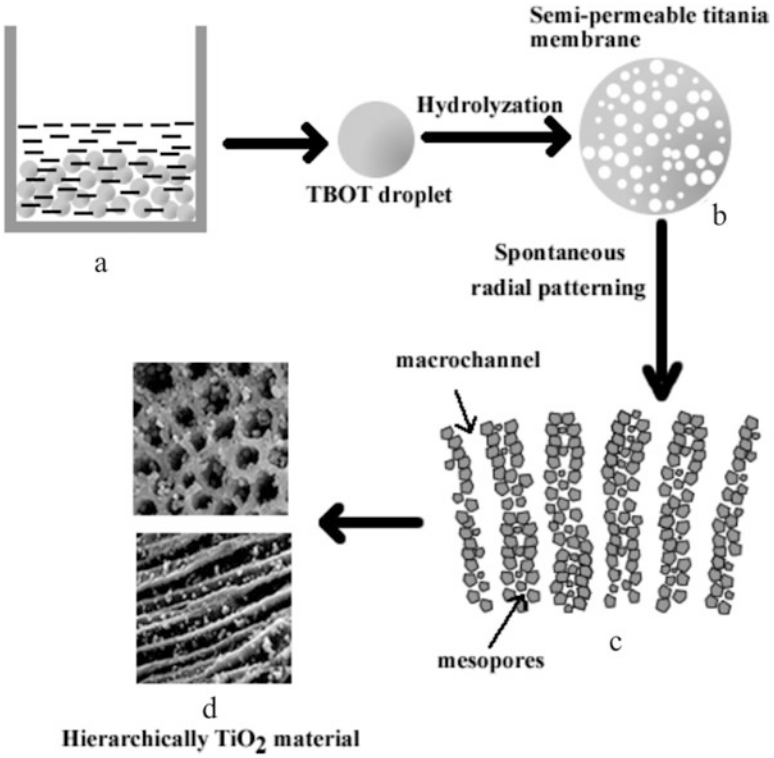

Fig. 9.3 Schematic procedure for the formation mechanism of the hierarchical macro-/mesoporous titania (Reproduced from ref. [7] by permission of John Wiley & Sons Ltd)

immediately produces a thin, dense semipermeable titania membrane at the droplet interface. Then, the distilled water diffuses through the spherical outer membrane, and the reaction proceeding inwards is approximately perpendicular to the external surface of the particles. The water/alcohol channels within the TBOT droplets undergo spontaneous radial patterning caused by the hydrodynamic flow of the solvent. The calcination temperature has a strong effect on the structures and photocatalytic activity of the prepared titania. At 300 °C, the calcined sample shows the highest photocatalytic activity. The calcination temperature higher than 500 °C caused the destruction of the hierarchical macro-/mesoporous structure, thus leading to the decrease of the photocatalytic activity.

9.1.2 Hard-Template Route

Compared with template-free method, hard-template route allows higher tunability over the pore volume, layer numbers, and composition. SiO_2, carbon, and polymer

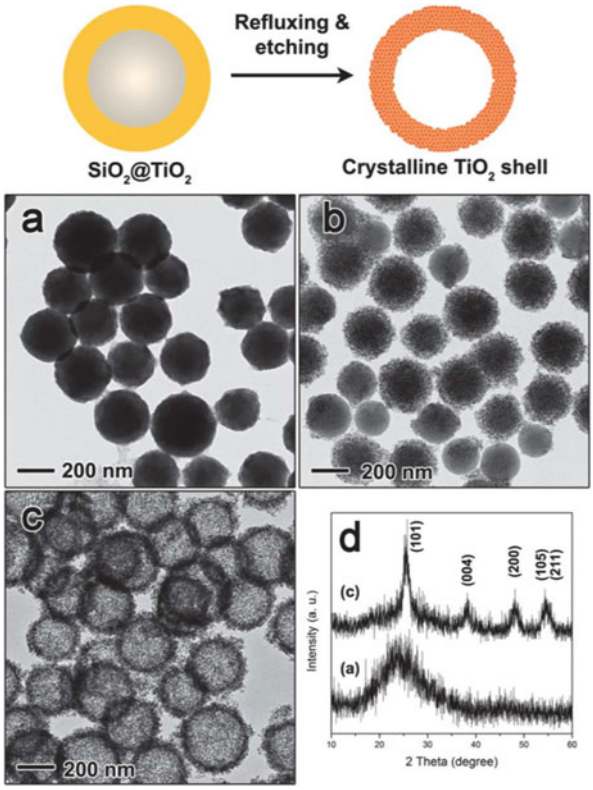

Fig. 9.4 Top: schematic illustration of the water-assisted crystallization strategy for converting an amorphous TiO_2 layer to mesoporous crystalline shells. Bottom, typical TEM images of the samples at each preparation step: (**a**) SiO_2@TiO_2 core–shell structures prepared by sol–gel coating; (**b**) SiO_2@TiO_2 core–shell structures after water-assisted crystallization; and (**c**) mesoporous TiO_2 hollow nanostructures after removing SiO_2 cores. (**d**) XRD patterns of samples (**a**) and (**c**), showing the transition from the amorphous to the anatase phase after water refluxing (Reproduced from ref. [8] by permission of John Wiley & Sons Ltd)

are the commonly used hard templates, which can be removed through acid–base etching, calcination, or dissolution. Yin et al. produced hollow TiO_2 using SiO_2 as the hard template [8], where amorphous TiO_2 was first coated around SiO_2 and then crystallized into anatase phase. SiO_2 was finally etched through NaOH to form interior void (Fig. 9.4).

Hierarchical macro-/mesoporous silica materials co-incorporated with Cr and Ti (MM–Si–Cr–Ti) were directly synthesized by adopting close-packed array of polystyrene (PS) microsphere as hard template for macropore and triblock copolymer Pluronic P123 as a soft template through a simple soaking-calcination way [9], where the Si/Ti ratio was fixed at 200 and Si/Cr ratio varied from 200 to 10. Ti specie is highly dispersed in the porous matrix, and Cr specie mainly exists as tetra-coordinated CrO_3 when Si/Cr $\leq$ 50 and transforms to a mixture of CrO_3 and crystallized hexa-coordinated Cr_2O_3 when the Si/Cr ratio is higher than 50 (Fig. 9.5).

Hierarchically ordered macro-/mesoporous TiO_2 films (denoted as H–TiO_2) with high thermal stability and crystallinity were synthesized using a confined evaporation-induced self-assembly (EISA) method [10]. P123 is used as a soft template to create the mesopores, and 3D periodic colloidal crystal PS are used as a hard template to create macropores (Scheme 9.1). The surfactant sulfuric acid

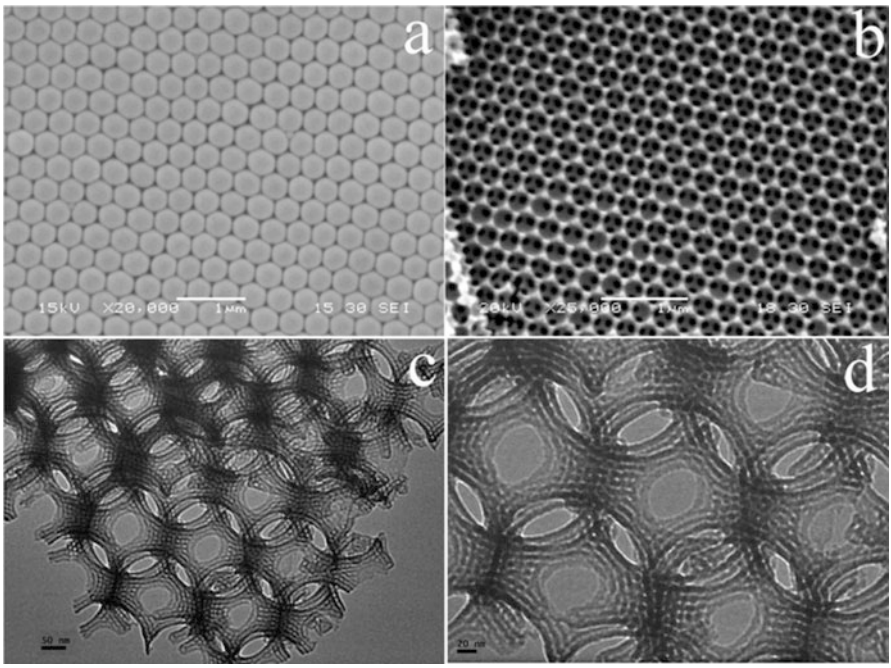

Fig. 9.5 SEM (**a**, **b**) and TEM (**c**, **d**) images of MM–Si–Cr–Ti prepared with molar ratio of Si–Cr–Ti = 200/10/1 (Reprinted from ref. [9], Copyright 2015, with permission from Elsevier)

carbonization method is applied to retain the ordered mesostructure during the high-temperature crystallization (550, 650 °C), while the PS spheres can generate amorphous carbon by heating treatment under an inert environment, which can support the inverse opal macrostructure from collapse. The hierarchically porous TiO_2 films present high surface areas of up to 240 $m^2\ g^{-1}$ and huge pore volume of ca. 1.2 $cm^3\ g^{-1}$. The photoelectrocatalytic water splitting performance of the hierarchical porous TiO_2 films is excellent and is much higher than that of pristine mesoporous TiO_2 films. The photoconversion efficiency is up to 5.23% for the N-doped hierarchically porous TiO_2 films.

9.2 Spatial Arrangement of Different Functions

The fabrication of yolk–shell structure allows the spatial arrangement of different functions. The Ostwald ripening process depicted in Fig. 9.1 can be used to encapsulate the metal core into the interior cavity. For example, Au/TiO_2 was fabricated through the following steps [11]: (1) formation of metallic cores, (2) aggregation of TiO_2 nanocrystallites around a single metallic core, (3) evacuation of central TiO_2 crystallites by Ostwald ripening, and (4) manipulation of the metal

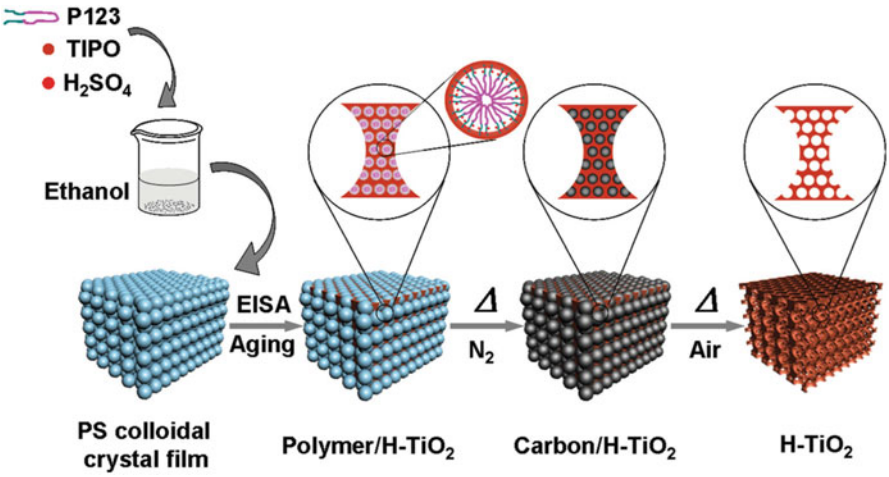

Scheme 9.1 Scheme of the synthesis process of the hierarchically ordered macro-/mesoporous TiO_2 films. The Ti precursor solution containing triblock copolymer Pluronic P123 and H_2SO_4 was impregnated into the interspace of the PS colloidal crystal films. After an EISA and aging process, the as-formed polymer–H–TiO_2 composite films were calcined under N_2 atmosphere at a high temperature (400, 550, 650 °C), and the in situ carbon that came from the carbonization of PS spheres and Pluronic P123 was generated both in macropores and mesopores to form the carbon–H–TiO_2 composite films. After the calcination in air to remove the carbon, the hierarchically ordered macro-/mesoporous TiO_2 films (H–TiO_2) with high crystallinity could be obtained (Reproduced from ref. [10] by permission of John Wiley & Sons Ltd)

core to a desired size via controlling the growth of the inside metal. For the size manipulation, $HAuCl_4$ was first introduced into the vacant space of the nanoreactor, and the $HAuCl_4$-soaked Au/TiO_2 nanoreactors were then placed in a solution of cetyltrimethylammonium bromide (CTAB) and ascorbic acid. It is believed that a slow interdiffusion between the $HAuCl_4$ inside the nanoreactor and the CTAB/ascorbic acid solution outside the nanoreactor would ensure a slow growth of Au cores while preventing TiO_2 shells from direct metal deposition. The size of Au core can be tuned in the range of 150–250 nm (Figs. 9.6 and 9.7).

Li et al. reported a facile "hydrothermal etching assisted crystallization" route to synthesize Fe_3O_4@titanate yolk–shell microspheres with ultrathin nanosheets-assembled double-shell structure [12]. The as-prepared microspheres possess a uniform size, tailored shell structure (Fig. 9.8), good structural stability, versatile ion-exchange capability, high surface area, and large magnetization and exhibit a remarkable photocatalytic performance.

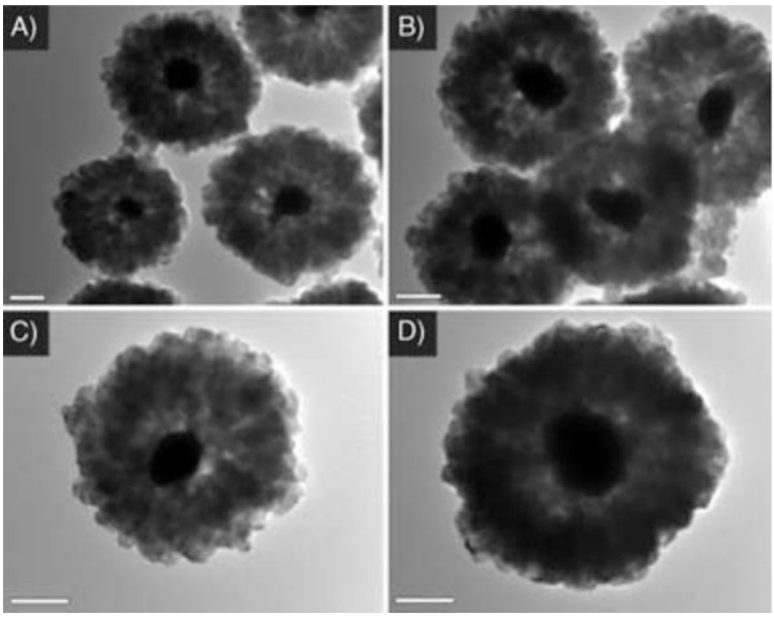

Fig. 9.6 (**a**)–(**d**) TEM images of Au/TiO_2 core–shell nanoreactors after enlargement of Au cores. All bar scales: 200 nm (Reprinted with the permission from ref. [11]. Copyright 2007 American Chemical Society)

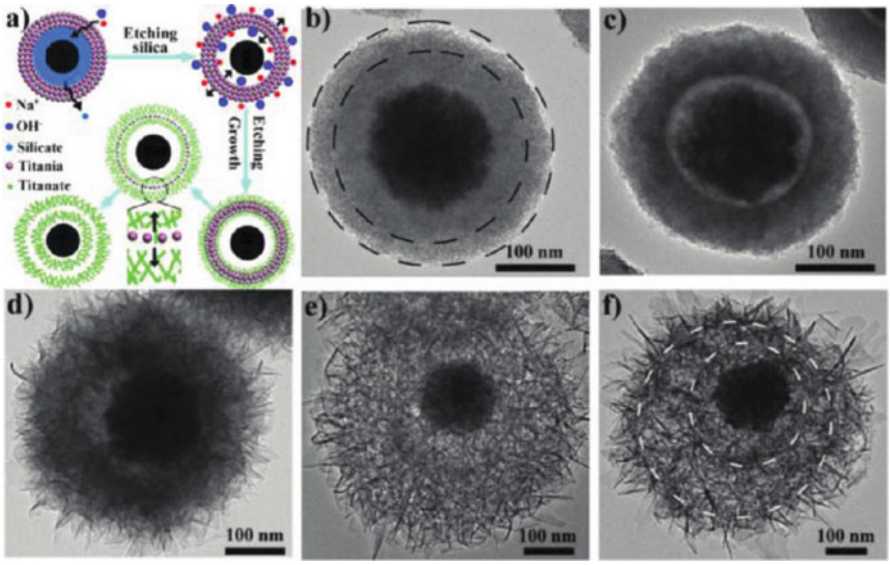

Fig. 9.7 (**a**) Schematic illustration of the "hydrothermal etching assisted crystallization" strategy for the formation of the Fe_3O_4@titanate double-shelled yolk–shell microspheres. TEM images of a single sphere synthesized at 150 C with hydrothermal treatment time: (**b**) 0 min, (**c**) 20 min, (**d**) 2 h, (**e**) 12 h, and (**f**) 24 h (Reprinted with the permission from ref. [12]. Copyright 2011 American Chemical Society)

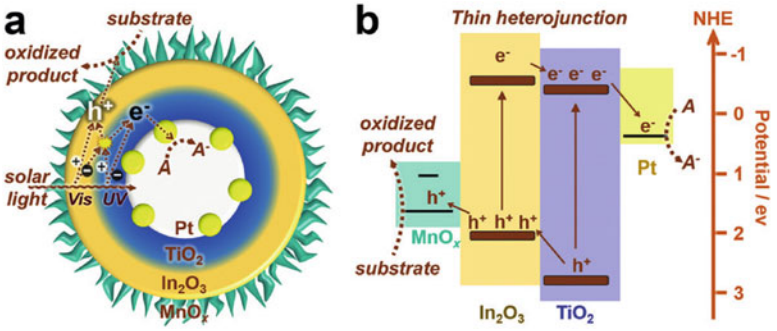

Fig. 9.8 The PTIM-MS structure and the mechanism for photocatalytic oxidation. Pt and MnOx are spatially separated by the TiO_2–In_2O_3 heterogeneous double-layered shell. (**a**) The reaction process. A represents an electron acceptor; here, $NaIO_3$ was used. (**b**) Simplified band structure of the catalyst. The CB positions of In_2O_3 and TiO_2 are 0.63 and 0.40 eV vs NHE, and the VB positions of In_2O_3 and TiO_2 were calculated to be 2.17 and 2.80 eV vs NHE according to the corresponding bandgaps (Reproduced from ref. [14] by permission of John Wiley & Sons Ltd)

9.3 Acceleration of Photo-Carrier Separation

Submicrometer-sized yolk–shell-structured Au@TiO_2 was synthesized by controllably hydrolyzing TiF_4 in Au nanoparticle solution under hydrothermal condition [13]. Both the size and the shell thickness could be easily adjusted by changing the amount of TiF4 in reaction mixture. Notably, when these Au@TiO2 hollow submicrospheres were used as the working electrodes for DSSCs, an obvious improvement in conversion efficiency is achieved compared to those solar cells based on TiO2 hollow spheres or TiO2 nanoparticles. DSSCs fabricated with Au–P25 composite materials and Au/TiO_2 core–shell nanowires can achieve an efficiency of 3.3% and 4.53%, respectively. As comparison, Au@TiO_2 hollow submicrospheres achieve a remarkably higher efficiency of 8.13%. Such a large enhancement should be ascribed to the fact that the sealed Au particles in the TiO_2 shells can effectively suppress both back electron transfer and energy transfer from dye to Au particles (Scheme 9.2).

Pt@TiO_2@In_2O_3@MnO_x mesoporous hollow spheres (PTIM-MSs) was designed and synthesized as shown in Fig. 9.8, which combine the advantages of spatially separated cocatalysts (Pt and MnO_x) and thin heterojunctions (TiO_2@In_2O_3 shell) to simultaneously reduce bulk and surface recombination [14]. Spatially separated cocatalysts drive electrons and holes near the surface to flow in opposite directions, reducing their recombination. Thin heterojunctions can effectively separate charges in the bulk phase and enable their transfer to the surface–subsurface region where they can be easily trapped by cocatalysts for surface reactions. Furthermore, In_2O_3 serves as a sensitizer to enhance light absorption. In combination with other advantages, such as a large surface area, long light-scattering path, and surface reaction kinetics promoted by cocatalysts, the PTIM-MS system is an

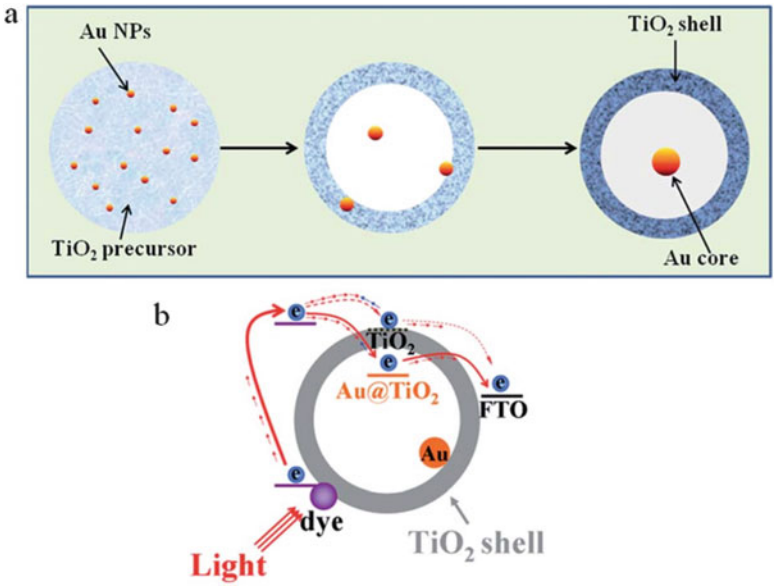

Scheme 9.2 Illustrations of (**a**) formation process of Au@TiO_2 hollow submicrospheres and (**b**) the charge separation process in the DSSCs with the photoanode of Au@TiO_2 hollow submicrospheres (Reproduced from ref. [13] by permission of John Wiley & Sons Ltd)

excellent photocatalyst of both water oxidation and selective benzyl alcohol oxidation.

A new strategy for design and synthesis of Co_9S_8 hollow cubes decorated by CdS QDs was developed by Zhang et al. [15]. The hybrid Z-scheme system is obtained by a simple hydrothermal method containing dimethyl sulfoxide (DMSO) as a solvent and hollow $Co(OH)_2$ cubes as a template. DMSO solvent served as a sulfur source to react with Cd^{2+}, producing CdS QDs, and was also used as the anion exchange reagent to react with easily prepared $Co(OH)_2$ cubes. The hollow CdS–Co_9S_8 cubes exhibit efficient solar light harvesting, as well as impressively enhanced hydrogen evolution reaction (HER) activity and stability under solar light irradiation compared to that of the pure Co_9S_8 and CdS catalysts. An efficient Z-scheme building block and the multiple reflections of solar light within the cavity of hollow cubes are responsible for substantially enhanced HER activity and stability (Fig. 9.9).

MnO_x@CdS/CoP hollow spheres with spatially separated surfaces were fabricated by loading the dual cocatalysts (inside MnO_x and outside CoP) for enhanced photocatalytic H_2 evolution activities [16]. CdS shells (hollow spheres) can be realized by using SiO_2 spheres as sacrificial templates, where the MnO_x and CoP NPs are selectively anchored on the inner and outer surface of CdS shells, respectively. That is, the photo-generated electrons and holes can directionally migrate to the locations of dual cocatalysts for reduction and oxidation reaction, respectively.

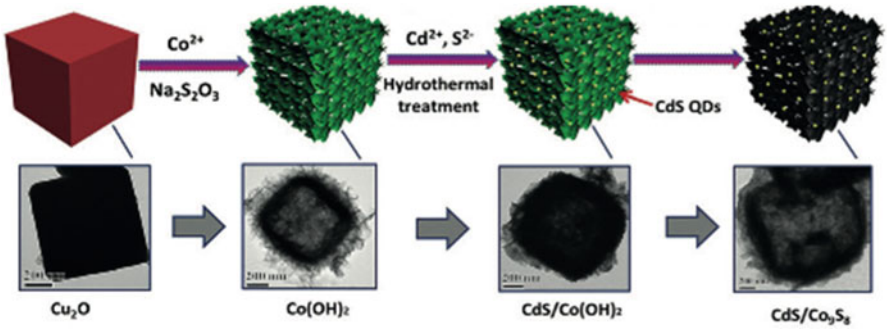

Fig. 9.9 The preparative process for CdS–Co_9S_8 and corresponding TEM images; scale bar = 200 nm (Reproduced from ref. [15] by permission of John Wiley & Sons Ltd)

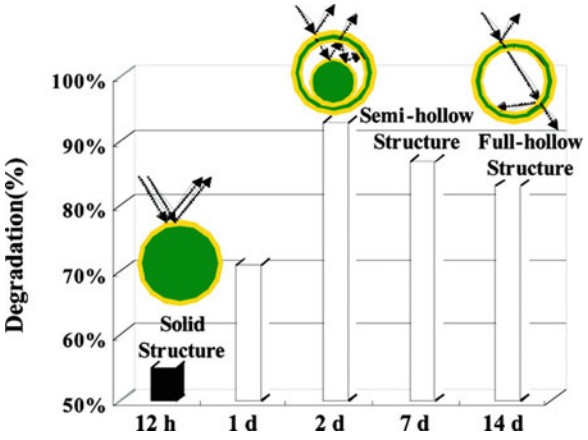

Fig. 9.10 Comparison of photocatalytic activities of the titania spheres with solid, sphere-in-sphere, and hollow structure. Inset shows a schematic illustration of multireflections within the sphere-in-sphere structure (Reprinted with the permission from ref. [6]. Copyright 2007 American Chemical Society)

As expected, in this case, the recommendation of electrons and holes has been significantly restrained, and the MnO_x@CdS/CoP catalyst shows a reduction surface and an enhanced photocatalytic activity for H_2 evolution (Fig. 9.10).

9.4 Multiple Light Scattering

The hollow or yolk–shell structure allows the multiple reflections of incident light within the interior cavity, thus enhancing the photocatalytic activity due to the improved light absorption efficiency (Fig. 9.11) [6]. The destroying of sphere-in-sphere structure by grinding the spheres causes a dramatic decrease of photocatalytic activity that is similar to that of the solid spheres. As schematically illustrated in the inset, a sphere-in-sphere structure with an appropriate inner sphere diameter allows

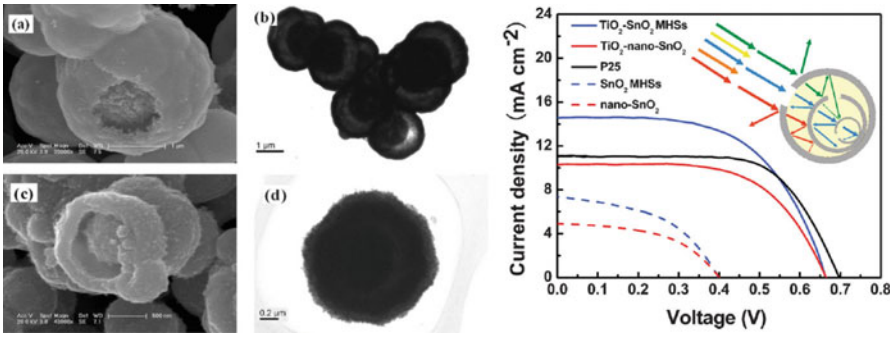

Fig. 9.11 (Left) SEM and (b) HRTEM images of SnO_2 MHSs. (c) SEM and (d) HRTEM images of TiO_2–SnO_2 MHSs. (Right) I–V characteristics of DSSCs with the photoelectrode films of TiO_2–SnO_2 MHSs, TiO_2–nano-SnO_2, SnO_2 MHSs, nano-SnO_2, and TiO_2 (P25) nanoparticles. The inset illustrates the multiple reflecting and scattering of light in the multilayered hollow spheres (Reproduced from ref. [16] by permission of John Wiley & Sons Ltd)

more efficient use of the light source and therefore offers an improved catalytic activity. The hollow and yolk–shell structures with smaller inner spheres show lower activity due to the reduced light reflection efficiency.

Qian et al. designed TiO_2-coated multilayered SnO_2 hollow microspheres (MHS) for dye-sensitized solar cells [16]. Multilayered spherical SnO_2–C composite was first formed through a condensation polymerization and carbonization of sucrose accompanied by hydrolysis of $SnCl_4$ in the hydrothermal reaction. Then, hollow SnO_2 were obtained by removal of carbon via calcination. Compared to TiO_2, SnO_2 has higher electron mobility and larger bandgap. However, SnO_2-based DSSCs generally have lower conversion efficiencies than TiO_2, which are attributed to a faster interfacial electron recombination and lower trapping density. On the other hand, SnO_2 has a lower isoelectric point (pH = 4–5) than anatase TiO2 (pH = 6–7), which leads to less adsorption of the dye with acidic carboxyl groups. To solve these problems, coating a thin layer of an isolating oxide, such as TiO_2, ZnO, Al2O3, or MgO, has been adopted to improve the conversion efficiency of SnO_2 photoelectrodes. TiO_2–SnO_2 multilayered hollow microspheres (SnO_2 MHSs) were synthesized by two steps (Fig. 9.8). First, SnO_2 MHSs were prepared by a chemically induced self-assembly reaction of aqueous sucrose–$SnCl_4$ solution under hydrothermal condition. The second step was to coat TiO_2 nanocrystallites onto the SnO_2 MHSs by impregnating in TiCl4 and then hydrolyzing $TiCl_4$ to form a surface layer of TiO_2.

The distinct photovoltaic behavior of the TiO_2–SnO_2 MHSs is its large short-circuit current (JSC, 14.6 mA cm^{-2}) compared with TiO_2–nano-SnO_2 (J_{SC}, 10.3 mA cm^{-2}) and TiO_2 (J_{SC}, 11.1 mA cm^{-2}) nanoparticles. This enhanced photocurrent could be attributed to better dye adsorption, due to increased active surface area, or better light-harvesting efficiency, due to the hollow spherical structure. Since the amount of dye adsorption on the TiO_2–SnO_2 MHSs is very similar to those of TiO_2–nano-SnO_2 and TiO_2 nanoparticles, the larger JSC value for

the TiO_2–SnO_2 MHSs is most likely given rise by an enhanced light harvesting due to multiple light reflecting and scattering in between the hierarchical spherical shells of the TiO_2–SnO_2 MHSs, rather than an increased surface area. The JSC value for the SnO_2 MHSs is 50% higher than that of nano-SnO_2, suggesting that the enhanced JSC value for the TiO_2–SnO_2 MHSs compared with the TiO_2–nano-SnO_2 is due to the hierarchical spherical structure rather than the $TiCl_4$ treatment. The inset in Fig. 9.11 (right) illustrates the reflecting and scattering of light in a TiO_2–SnO_2 MHS. It is believed that the shells with the different sizes in a microsphere cannot only multireflect but also scatter the incident light of different wavelengths in the range of visible light. The improved photocurrent for the TiO_2–SnO_2MHSs is mainly contributed to its multilayered hollow spherical structure, which provides an effective way to enhance light-harvesting efficiency.

Photonic-crystal-based optical coupling offers a unique way of light–matter interaction to increase light harvesting, especially around the absorption edge of a semiconductor. A photonic crystal is a periodic dielectric structure that can forbid the propagation of light in a certain crystal direction within a certain spectrum regime, called a photonic stop-band. The light in a photonic crystal undergoes strong coherent multiple scattering and travels with very low group velocity near the photonic stop-band edges, referred to as slow light. Such a slow-light effect can considerably increase the effective optical path length, therefore leading to a delay and storage of light in photonic materials. 3D photonic crystal design was utilized to enhance incident photon-to-electron conversion efficiency (IPCE) of WO3 photoanodes. Large-area and high-quality WO3 photonic crystal photoanodes with inverse opal structure were prepared (Fig. 9.12). The photonic stop-bands of these WO3 photoanodes were tuned experimentally by variation of the pore size of inverse opal structures. It was found that when the red edge of the photonic stop band of WO3 inverse opals overlapped with the WO3 electronic absorption edge at Eg = 2.6–2.8 eV, a maximum of 100% increase in photocurrent intensity was observed under visible light irradiation ($\lambda > 400$ nm) in comparison with a disordered porous WO3 photoanode (Fig. 9.13). When the red edge of the stop band was tuned well within the electronic absorption range of WO3, noticeable but less amplitude of enhancement in the photocurrent intensity was observed. It was further shown that the spectral region with a selective IPCE enhancement of the WO3 inverse opals exhibited a blueshift in wavelength under off-normal incidence of light, in agreement with the calculated stop band edge locations. The enhancement could be attributed to a longer photon– matter interaction length as a result of the slow-light effect at the photonic stop-band edge, thus leading to a remarkable improvement in the light-harvesting efficiency. The present method can provide a potential and promising approach to effectively utilize solar energy in visible light-responsive photoanodes [17].

A range of TiO_2 inverse opals with tunable macroporous size were synthesized using different sized PS arrays as hard templates [18]. After a simple heating treatment in vacuum, Ti^{3+}-doped TiO_2 inverse opals were obtained. The optical responses of TiO_2- and Ti^{3+}-doped TiO_2 inverse opals could be enhanced by choosing PS arrays with appropriate size as hard templates due to the slow light

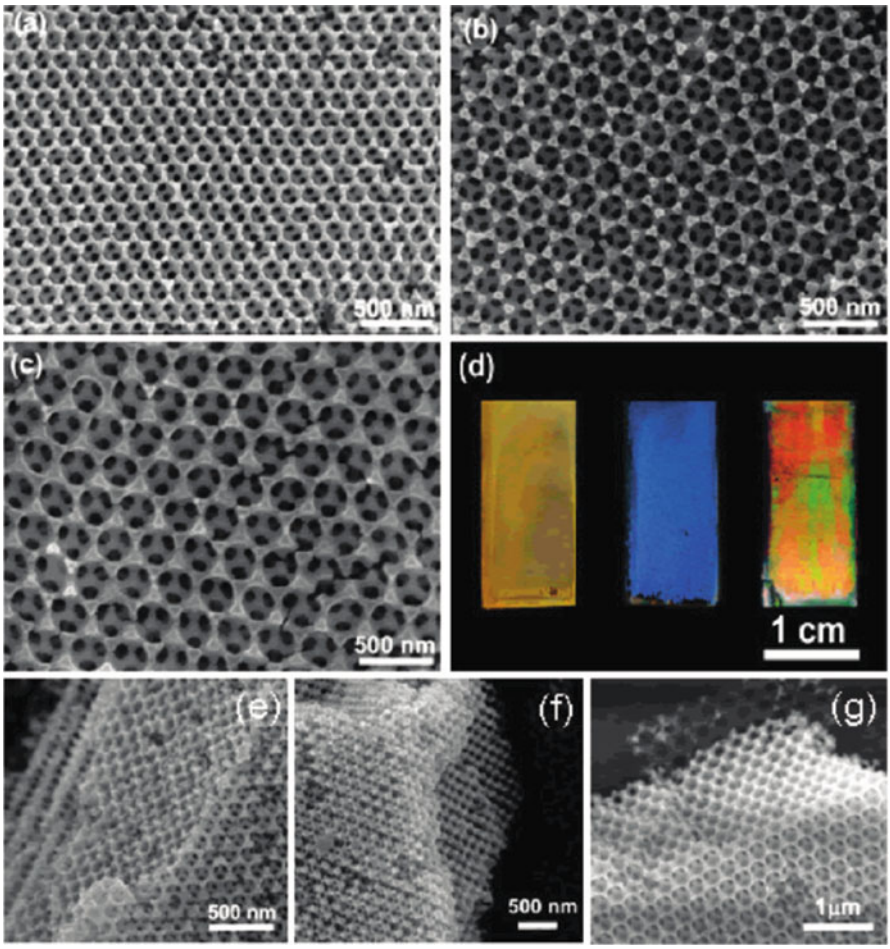

Fig. 9.12 SEM images of WO_3 inverse opals: (**a**) WO_3-200, (**b**) WO_3-260, and (**c**) WO_3-360. (**d**) Photograph of the inverse opal WO_3 photoanodes under white light illumination, WO_3-200, WO_3-260, and WO_3-360, from left to right. (**e–g**) SEM images of cross-sectional view of each inverse opal. The thickness is estimated to be about 2.5 μm (17 layers) for WO_3-200 (**e**), 2.6 μm (14 layers) for WO_3-260 (**f**), and 2.7 μm (11 layers) for WO_3-360 (**g**) (Reprinted with the permission from ref. [17]. Copyright 2011 American Chemical Society)

effect of inverse opal structure, thus coupling the physical and chemical enhancement for the light absorption. The photocatalytic efficiency was evaluated by the photodegradation of AO7, and it is proved that the cooperation of slow light effect and Ti^{3+} doping is an effective way to improve visible light-driven photocatalytic performance of TiO_2 photocatalyst (Scheme 9.3).

To achieve the coupling between the slow photon effect and plasmon resonance absorption, three-dimensional ordered assembly of TiO_2 hollow nanospheres deposited with Au nanoparticles (Au/TiO_2–3DHNSs) was designed (Fig. 9.14) [19]. A

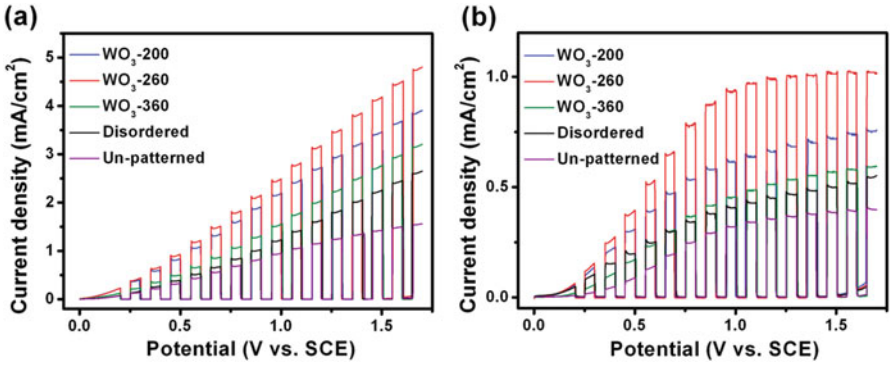

Fig. 9.13 Photocurrent potential curves of different WO_3 photoanodes measured under (**a**) UV–visible light irradiation ($\lambda > 300$ nm) and (**b**) visible light irradiation ($\lambda > 400$ nm) (Reprinted with the permission from ref. [17]. Copyright 2011 American Chemical Society)

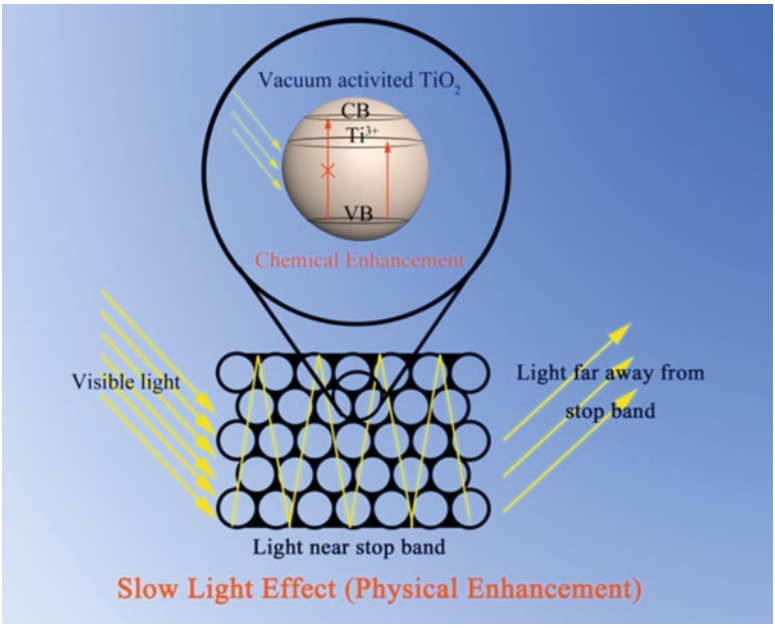

Scheme 9.3 Scheme of slow light effect (physical enhancement) and vacuum activation (chemical enhancement) (Reprinted from ref. [18], Copyright 2014, with permission from Elsevier)

photonic stop band centered at 500 nm was observed from the reflection spectrum (Fig. 9.15). As such, the slow photon effect occurring at the edges of the stop band is expected to appear in the range of 550–620 nm, which matches well with the surface plasmon resonance (SPR) absorption of Au nanoparticles. The wavelength matching of SPR absorption and photonic band edge would be expected to increase the SPR

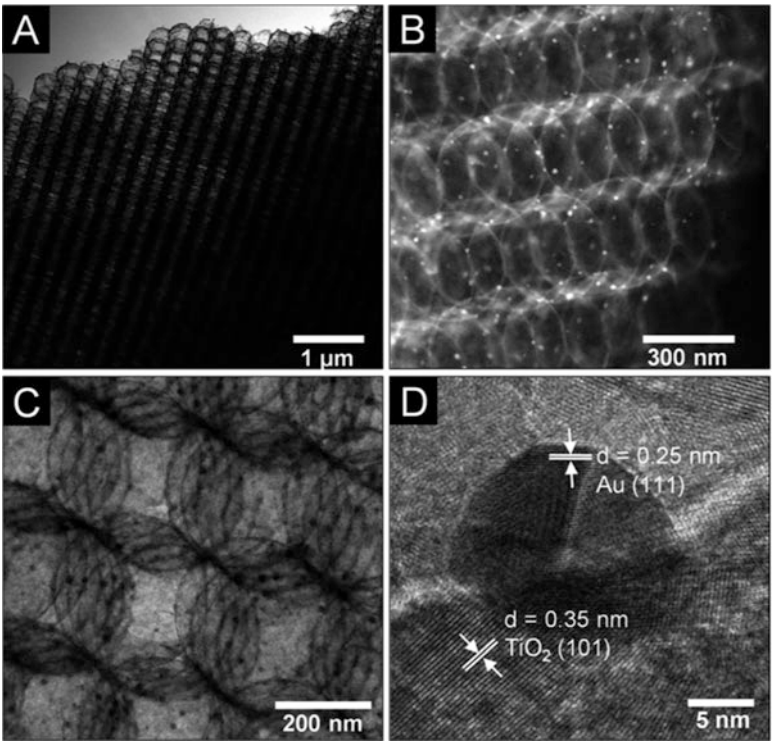

Fig. 9.14 (**a**) TEM; (**b**) STEM; (**c**, **d**) HRTEM images of Au/TiO_2–3DHNSs (Reproduced from ref. [19] by permission of John Wiley & Sons Ltd)

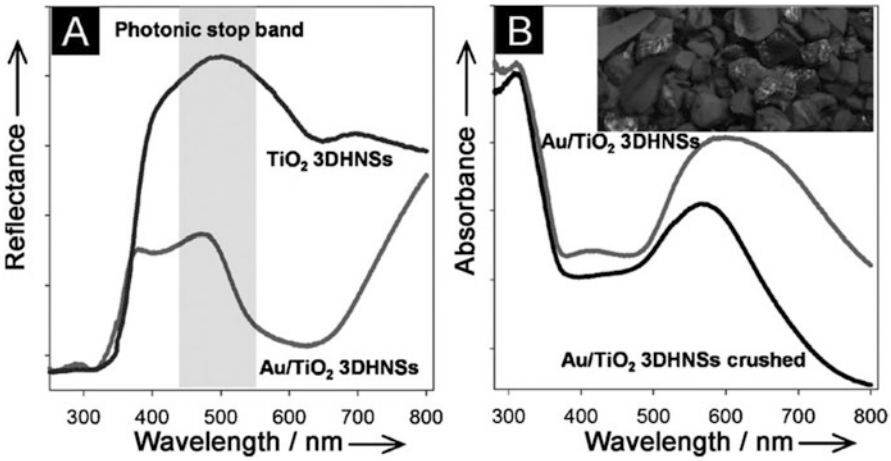

Fig. 9.15 (**a**) UV–vis diffuse reflectance spectra for Au/TiO_2–3DHNSs and the TiO_2–3DHNSs reference sample. The shaded region in (A) shows the presence of photonic stop band. (**b**) UV–vis absorption spectra of Au/TiO_2–3DHNSs before and after being crushed. Inset in (B) shows a digital photo of Au/TiO_2–3DHNSs (Reproduced from ref. [19] by permission of John Wiley & Sons Ltd)

intensity since an increase of the effective path length of light in the photonic band edge regions would result in a significant enhancement of the interaction between photons and Au NPs, which was verified by the decreased SPR absorption from crushed microarray structures (Fig. 9.14).

The photocatalytic activity of Au/TiO_2–3DHNSs for the decomposition of isopropanol to CO_2 under visible light illumination ($\lambda = 420$ nm) was investigated using Au/TiO_2–P25, crushed Au/TiO_2–3DHNSs, and Au/TiO_2–HNSs without the 3D ordered structure as the reference samples. Among all of samples, CO_2 produced from Au/TiO_2–3DHNSs is much higher than those from other samples. Therefore, the 3D ordered assembly of HNSs with periodic voids exhibits the slow photon effect which enhances the visible light absorption and, as a consequence, increases the photocatalytic activity of Au/TiO_2–3DHNSs. Even under the UV light irradiation, Au/TiO_2–3DHNSs still show the highest activity, which can be mainly attributed to the multiple light scattering resulting from the unique 3DHNS structure.

References

1. Yin YD, Rioux RM, Erdonmez CK et al (2004) Formation of hollow nanocrystals through the nanoscale Kirkendall effect. Science 304:711–714
2. Yang HG, Zeng HC (2004) Preparation of hollow anatase TiO_2 nanospheres via Ostwald ripening. J Phys Chem B 108:3492–3495
3. Wang X, Feng J, Bai Y et al (2016) Synthesis, properties, and applications of hollow micro-/nanostructures. Chem Rev 116:10983–11060
4. Li J, Zeng HC (2005) Size tuning, functionalization, and reactivation of Au in TiO_2 nanoreactors. Angew Chem Int Ed 44:4342–4345
5. Wang PH, Yang LG, Wang LZ et al (2016) Template-free synthesis of hollow anatase TiO_2 microspheres through stepwise water-releasing strategy. Mater Lett 164:405–408
6. Li H, Bian Z, Zhu J et al (2007) Mesoporous Titania spheres with tunable Chamber structure and enhanced photocatalytic activity. J Am Chem Soc 129:8406–8407
7. Yu JG, Su YR, Cheng B (2007) Template-free fabrication and enhanced photocatalytic activity of hierarchical macro-/mesoporous Titania. Adv Funct Mater 17:1984–1990
8. Joo JB, Lee I, Dahl M et al (2013) Controllable synthesis of mesoporous TiO_2 hollow shells: toward an efficient photocatalyst. Adv Funct Mater 23:4246–4254
9. Lu LJ, Teng F, Sen T et al (2015) Synthesis of visible-light driven Cr_xO_y–TiO_2 binary photocatalyst based on hierarchical macro–mesoporous silica. Appl Cata B Environ 163:9–15
10. Zhang RY, Shen DK, Xu M et al (2014) Ordered macro-/mesoporous anatase films with high thermal stability and crystallinity for photoelectrocatalytic water-splitting. Adv Energy Mater 4:1301725
11. Li J, Zeng HC (2007) Hollowing Sn-Doped TiO_2 nanospheres via Ostwald Ripening. J Am Chem Soc 129:15839–15847
12. Li W, Deng Y, Wu ZX et al (2011) Hydrothermal etching assisted crystallization: a facile route to functional yolk-shell titanate microspheres with ultrathin nanosheets-assembled double shells. J Am Chem Soc 133:15830–15833
13. Li A, Chang X, Huang Z et al (2016) Thin heterojunctions and spatially separated cocatalysts to simultaneously reduce bulk and surface recombination in photocatalysts. Angew Chem Int Ed 55:13734–13738
14. Qiu B, Zhu Q, Du M et al (2017) Efficient solar light harvesting CdS/Co_9S_8 hollow cubes for Z-scheme photocatalytic water splitting. Angew Chem Int Ed 129:2728–2732

15. Xing M, Qiu B, Du M et al (2017) Spatially separated CdS shells exposed with reduction surfaces for enhancing photocatalytic hydrogen evolution. Adv Funct Mater 27:1702624
16. Qian J, Liu P, Xiao Y et al (2009) TiO_2-Coated multilayered SnO_2 hollow microspheres for dye-sensitized solar cells. Adv Mater 21:3663–3667
17. Chen X, Ye J, Ouyang S et al (2011) Enhanced incident photon-to-electron conversion efficiency of tungsten trioxide photoanodes based on 3D-photonic crystal design. ACS Nano 5:4310–4318
18. Qi DY, Lu LJ, Xi ZH et al (2014) Enhanced photocatalytic performance of TiO_2 based on synergistic effect of Ti3+ self-doping and slow light effect. Appl Catal B Environ 160–161:621–628
19. Dinh CT, Yen H, Kleitz F et al (2014) Three-dimensional ordered assembly of thin-shell Au/TiO_2 hollow nanospheres for enhanced visible-light-driven photocatalysis. Angew Chem Int Ed 53:6618–6623